Experimental report

16/08/2021

Proposal: 5-53-289 **Council:** 10/2019

Title: Temperature dependence of microstructural-defect-induced Dzyaloshinskii-Moriya interaction

Research area: Physics

This proposal is a continuation of 5-53-283

Main proposer: Mathias BERSWEILER

Experimental team: Mathias BERSWEILER
Nina-Juliane STEINKE
Philipp BENDER
Yojiro OBA

Local contacts: Nina-Juliane STEINKE

Samples: Tb

Instrument	Requested days	Allocated days	From	To
D33	5	4	10/09/2020	14/09/2020

Abstract:

Recently, we have experimentally and theoretically demonstrated that the DMI influences the magnetic microstructure of polycrystalline magnetic materials exhibiting a large defect density (e.g. grain boundaries or dislocations). Microstructural defects act as a source of additional local chiral interactions due to the symmetry breaking at the defect sites, similar to the intrinsic DMI in noncentrosymmetric crystals such as MnSi. The signature of this effect is a characteristic asymmetry in the polarized SANS cross section. In this continuation work, we will explore the temperature dependence of the defect-induced DMI by carrying out polarized SANS experiments on a 21nm-sized nanocrystalline terbium sample (with a high density of grain boundaries). The outcome of this experiment will contribute to our fundamental understanding of polarized magnetic SANS and one will learn on the defect-related DMI mechanism.

Revealing defect-induced spin disorder in nanocrystalline Ni

Mathias Bersweiler,[1] Evelyn Pratami Sinaga,[1] Inma Peral,[1] Nozomu Adachi,[2] Philipp Bender,[3] Nina-Juliane Steinke,[4] Elliot Paul Gilbert,[5] Yoshikazu Todaka,[2] Andreas Michels,[1] and Yojiro Oba,[6]

[1] *Department of Physics and Materials Science, University of Luxembourg, 162A Avenue de la Faïencerie, L-1511 Luxembourg, Grand Duchy of Luxembourg*
[2] *Department of Mechanical Engineering, Toyohashi University of Technology, 1-1 Hibarigaoka, Tempaku, Toyohashi, Aichi 441-8580, Japan*
[3] *Heinz Maier-Leibnitz Zentrum (MLZ), Technische Universität München, D-85748 Garching, Germany*
[4] *Institut Laue-Langevin, 71 avenue des Martyrs, F-38042 Grenoble, France*
[5] *Australian Centre for Neutron Scattering, Australian Nuclear Science and Technology Organization, Locked Bag 2001, Kirrawee DC, New South Wales 2232, Australia*
[6] *Materials Sciences Research Center, Japan Atomic Energy Agency, 2-4 Shirakata, Tokai, Ibaraki 319-1195, Japan*

1. Introduction

Ultrafine-grained and nanocrystalline magnetic materials have attracted considerable interest over the last decades owing to their large potential for technological applications [1–4]. Among the most well-known and efficient techniques for synthesizing such materials are inert-gas condensation and high-pressure torsion (HPT), the latter being a severe plastic deformation method. For a brief overview of the main techniques for the preparation of bulk ultrafine-grained and nanocrystalline materials, we refer the reader to the article by Koch [5]; a detailed review on the HPT technique can be found in Ref. [6].

Since the magnetic properties will ultimately determine the performance of ultrafine-grained materials, a precise knowledge of the relationship between the microstructure and the magnetic properties, *i.e.*, the correlation between *e.g.* the saturation magnetization, coercive field, and magnetic anisotropy and the average grain size or crystallographic texture is crucial. Previous studies have reported that the magnetic properties of strained nanocrystalline materials produced by HPT strongly differ from polycrystalline samples with larger grain sizes; in particular, a reduction of the saturation magnetization (by 5 %) and a significant increase of the coercive field (~ 50 times larger) were observed in HPT Ni using magnetometry [7]. These features were qualitatively explained, respectively, by the decrease of the exchange energy in the vicinity of defects [8] and by the increase of the dislocation density within the grain boundaries [7]. The investigation of the magnetic domain structure of HPT materials with the aim to clarify the magnetization reversal mechanism has been mainly performed using Lorentz electron microscopy [9,10]. Although these studies reported that the domain structure (*i.e.*, shape and size) is not strongly affected by the grain size, the influence of a high density of lattice defects (*e.g.* vacancies, dislocations, grain boundaries, pores) induced by HPT on the spin structure still needs to be further clarified. As previously demonstrated, HPT can be used to modify the structure and thus to control the *macroscopic* magnetic properties of magnetic materials [11,12]. Therefore, in the context of defect engineering of advanced materials using severe plastic deformation [13], a better understanding of the influence of the defects on the magnetic properties at different length scales is necessary.

In this study we employ unpolarized magnetic small-angle neutron scattering (SANS) to investigate the magnetic microstructure of HPT Ni on the *mesoscopic* length scale. Magnetic SANS is a powerful technique which provides volume-averaged information about the perturbation of the magnetization vector field on a length scale of about 1 – 500 nm (see Refs. [14,15] for reviews of the magnetic SANS fundamentals and applications). This technique was recently used to demonstrate that in HPT Fe defects act as a source of an anomalous effective magnetic anisotropy field [16]. Here, we go a step further in the neutron data analysis. We determine the real-space magnetic correlation lengths from the magnetic SANS data to obtain estimates for the average defect size as well as for the spatial extent of the surrounding spin disorder within the bulk of the sample. The specific neutron data analysis of the spin misalignment brings additional information which is important for the understanding of the role played by the defects in magnetic materials.

2. Magnetic SANS Analysis

2.1. *Unpolarized SANS cross section*

When the applied magnetic field is perpendicular to the incident neutron beam ($\boldsymbol{H}_0 \perp \boldsymbol{k}_0$), the elastic total (nuclear + magnetic) unpolarized SANS cross section $\mathrm{d}\Sigma/\mathrm{d}\Omega$ at momentum-transfer vector $\boldsymbol{q}$ can be written as [14, 15]:

$$\frac{d\Sigma}{d\Omega}(\boldsymbol{q}) = \frac{8\pi^3}{V} b_{\mathrm{H}}^2 \Big(b_{\mathrm{H}}^{-2} \big|\widetilde{N}\big|^2 + \big|\widetilde{M}_x\big|^2 + \big|\widetilde{M}_y\big|^2 \cos^2(\theta) + \big|\widetilde{M}_z\big|^2 \sin^2(\theta) - \big(\widetilde{M}_y \widetilde{M}_z^* + \widetilde{M}_y^* \widetilde{M}_z\big) \sin(\theta)\cos(\theta) \Big) \quad (1)$$

where V is the scattering volume, $b_H = 2.91 \times 10^8$ A^{-1}m^{-1} relates the atomic magnetic moment to the atomic magnetic scattering length, $\widetilde{N}(\boldsymbol{q})$ and $\widetilde{\boldsymbol{M}}(\boldsymbol{q}) = \big[\widetilde{M}_x(\boldsymbol{q}),\ \widetilde{M}_y(\boldsymbol{q}),\ \widetilde{M}_z(\boldsymbol{q})\big]$ represent the Fourier transforms of the nuclear scattering length density $N(\boldsymbol{r})$ and of the magnetization vector field $\boldsymbol{M}(\boldsymbol{r})$, respectively, θ specifies the angle between $\boldsymbol{H}_0$ and $\boldsymbol{q} \cong q\{0, \sin\theta, \cos\theta\}$ in the small-angle approximation, and the asterisks "*" denote the complex conjugated quantities. For small-angle scattering, the component of the scattering vector along the incident neutron beam, here q_x, is smaller than the other two components q_y and q_z, so that only correlations in the plane perpendicular to the incoming neutron beam are probed.

In our neutron-data analysis below, we subtract the SANS signal at the largest available field of 6.7 T [approach-to-saturation regime] from the measured data at lower fields. This subtraction procedure eliminates the nuclear SANS contribution $\propto \big|\widetilde{N}\big|^2$, which is field independent, and it yields the following purely magnetic SANS cross section $d\Sigma_{\mathrm{mag}}/d\Omega$:

$$\frac{d\Sigma_{\mathrm{mag}}}{d\Omega}(\boldsymbol{q}) = \frac{8\pi^3}{V} b_{\mathrm{H}}^2 \Big(\Delta\big|\widetilde{M}_x\big|^2 + \Delta\big|\widetilde{M}_y\big|^2 \cos^2(\theta) + \Delta\big|\widetilde{M}_z\big|^2 \sin^2(\theta) - \Delta\big(\widetilde{M}_y \widetilde{M}_z^* + \widetilde{M}_y^* \widetilde{M}_z\big) \sin(\theta)\cos(\theta) \Big) , \quad (2)$$

where the "Δ" stand for the differences of the Fourier components at the two fields considered. We emphasize that $d\Sigma_{\mathrm{mag}}/d\Omega$ is strongly dominated by the two transversal magnetization Fourier components $\widetilde{M}_{x,y}$.

2.2. *Magnetic correlation function*

The normalized magnetic correlation function $C(r, H_0)$ was numerically computed by a direct Fourier transformation of the experimental data for $\mathrm{d}\Sigma_{\mathrm{mag}}(q, H_0)/\mathrm{d}\Omega$ according to [17]:

$$C(r, H_0) = \frac{\int_0^\infty \frac{\mathrm{d}\Sigma_{\mathrm{mag}}(q, H_0)}{\mathrm{d}\Omega} j_0(qr) q^2 \mathrm{d}q}{\int_0^\infty \frac{\mathrm{d}\Sigma_{\mathrm{mag}}(q, H_0)}{\mathrm{d}\Omega} q^2 \mathrm{d}q} \quad , \quad (3)$$

where $j_0(qr) = \sin(qr)/qr$ is the zeroth-order spherical Bessel function. For this purpose, the experimental data $\mathrm{d}\Sigma_{\mathrm{mag}}(q, H_0)/\mathrm{d}\Omega$ beyond $q_{\max}$ were extrapolated to infinity using a power law, $\mathrm{d}\Sigma_{\mathrm{mag}}(q, H_0)/\mathrm{d}\Omega \propto 1/q^n$ with $4 \lesssim n \lesssim 7$ [compare inset in Fig. 1(b)], and the extrapolation from $q_{\min}$ to $q = 0$ was done according to $\mathrm{d}\Sigma_{\mathrm{mag}}(q, H_0)/\mathrm{d}\Omega \propto a + bq^2$.

2.3. *Magnetic correlation length*

The magnetic correlation length l_c characterizes the distance over which perturbations in the spin structure around a lattice defect are transmitted by the exchange interaction into the surrounding crystal lattice [18,19]. Several procedures for obtaining l_c are discussed in the literature, *e.g.*, $l_c(H_0)$ can be defined as the value of r for which $C(r,H_0) = C(0)e^{-1}$, or l_c can be found from the logarithmic derivative of $C(r,H_0)$ in the limit $r \to 0$ (Ref. [18]). Here, we determined the magnetic correlation length $l_c(H_0)$ from the $C(r,H_0)$ data at a particular field according to:

$$l_c(H_0) = \frac{\int_0^\infty rC(r,H_0)\mathrm{d}r}{\int_0^\infty C(r,H_0)\mathrm{d}r} \quad . \qquad (4)$$

The field dependence of the l_c data was then fitted using the following expression:

$$l_c(H_0) = \mathcal{L} + \sqrt{\frac{2A_{ex}}{\mu_0 M_s(H_0 + H^*)}} \quad , \qquad (5)$$

where the field-independent parameter $\mathcal{L}$ is of the order of the defect size, and A_{ex} and M_s are the exchange-stiffness constant and the saturation magnetization, respectively. The field H^* models the contribution of the magnetostatic and magnetic anisotropy field to the internal magnetic field. In the approach-to-saturation regime and for single-phase materials, where nonzero divergences of the magnetization from within the bulk are expected to be small [20], the main contributions to H^* are due to the magnetic anisotropy. The phenomenological model, Eq. (5), is based on micromagnetic theory [21,22] and expresses the relationship between the nuclear and magnetic microstructure of a material. Equation (5) has already been successfully used to describe the spin misalignments in several nanocrystalline bulk ferromagnetic materials [23,24]. To reduce the number of free parameters in the data analysis (see below), we fixed M_s to the value estimated from the magnetization curve, and A_{ex} to 8.5 pJ/m. This value is obtained by performing a global fit analysis of the field-dependent $\mathrm{d}\Sigma/\mathrm{d}\Omega$ data shown in Fig. 1(a) based on the micromagnetic SANS theory developed in Refs. [19,25]. The resulting volume-averaged value of $A_{ex} = 8.5 \pm 0.2$ pJ/m compares favorably with data reported for nanocrystalline Ni [22].

3. Results and discussion

Figure 1(a) displays the (over 2π) azimuthally-averaged total (nuclear + magnetic) SANS cross section $\mathrm{d}\Sigma(q,H_0)/\mathrm{d}\Omega$ measured at different applied magnetic fields. As can be seen, at the smaller momentum transfers q the cross section $\mathrm{d}\Sigma(q,H_0)/\mathrm{d}\Omega$ increases by more than two orders of magnitude when H_0 is decreased from 6.7 T to 0.1 T. Since the nuclear scattering is field independent, the strong field dependence of $\mathrm{d}\Sigma(q,H_0)/\mathrm{d}\Omega$ observed in Fig. 1(a) originates from spin-misalignment scattering caused by mesoscale spin disorder (*i.e.* from the failure of the spins to be completely aligned along $\boldsymbol{H}_0$). Figure 1(b) shows the corresponding purely magnetic SANS cross sections $\mathrm{d}\Sigma_{mag}(q,H_0)/\mathrm{d}\Omega$, which were obtained by subtracting the total scattering at 6.7 T (approaching saturation) from the data at lower fields. The magnitude of $\mathrm{d}\Sigma_{mag}(q,H_0)/\mathrm{d}\Omega$ is of the same order as $\mathrm{d}\Sigma(q,H_0)/\mathrm{d}\Omega$. The asymptotic power-law exponent n in $\mathrm{d}\Sigma_{mag}(q,H_0)/\mathrm{d}\Omega \propto 1/q^n$ was found to be larger than the value of n = 4 [see inset in Fig. 1(b)]; n = 4 would correspond to scattering from particles with sharp interfaces or from exponentially correlated fluctuations. The finding of a field-dependent n > 4 supports the notion of dominant spin-misalignment scattering, for which exponents n = 4–8 are theoretically predicted and experimentally found [14,23].

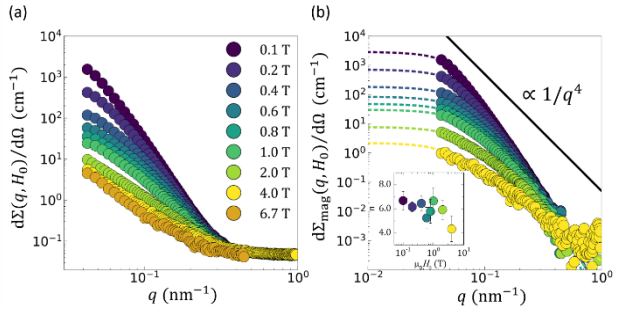

Figure 1: (a) Magnetic-field dependence of the (over 2π) azimuthally-averaged total (nuclear + magnetic) SANS cross section $\mathrm{d}\Sigma(q,H_0)/\mathrm{d}\Omega$ and (b) of the purely magnetic SANS cross section $\mathrm{d}\Sigma_{mag}(q,H_0)/\mathrm{d}\Omega$ (log-log scale). Dashed lines in (b): Extrapolation of $\mathrm{d}\Sigma_{mag}(q,H_0)/\mathrm{d}\Omega \propto 1/q^n$ from q_{max} to infinity and of $\mathrm{d}\Sigma_{mag}(q,H_0)/\mathrm{d}\Omega \propto a + bq^2$ from q_{min} to q = 0. Inset in (b): Field dependence of the asymptotic power-law exponent n of the magnetic SANS cross section $\mathrm{d}\Sigma_{mag}(q,H_0)/\mathrm{d}\Omega$ on a semi-logarithmic scale

Figure 2 shows the normalized magnetic correlation function $C(r,H_0)$, which was numerically computed according to Eq. (3). Increasing the field from 0.1 to 4 T results in a decrease of $C(r,H_0)$ at a given r. This observation reflects the decrease of the spin-misalignment fluctuations and the suppression of the amplitude of the static disorder with increasing field. Furthermore, the correlations do not decay exponentially (see the log-linear plot in the inset of Fig. 2), in agreement with the absence of a corresponding n = 4 power-law exponent observed in Fig. 1(b). Moreover, for the lowest applied fields, the absence of a finite slope of $C(r,H_0)$ in the limit $r \to 0$ is consistent with the absence of sharp interfaces in the magnetic microstructure and with the presence of a continuous magnetic scattering length density variation. By contrast, for homogeneous particles with a sharp interface (*i.e.*, with a discontinuous jump in the scattering-length density), the slope of the correlation function at the origin is finite and provides information on the fine structure of the particle (*e.g.*, on the surface-to-volume ratio). This is a direct consequence of the asymptotic q^{-4} Porod behavior of the SANS cross section (see the discussion by Porod in Ref. [26]). As shown in Ref. [17], for bulk ferromagnets, which are characterized by a smoothly-varying continuous magnetization vector field, the slope of $C(r)$ vanishes as $r \to 0$, and the asymptotic power-law behavior of the magnetic SANS cross section exhibits power-law exponents larger than n = 4.

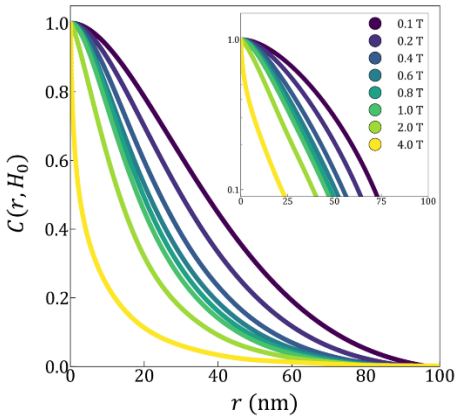

Figure 2: Magnetic-field dependence of the normalized magnetic correlation function $C(r,H_0)$. The correlation functions were numerically computed by a direct Fourier transformation [Eq. (3)] of $\mathrm{d}\Sigma_{mag}(q,H_0)/\mathrm{d}\Omega$ shown in Fig. 1(b). Inset: Plot of $C(r,H_0)$ on a semi-logarithmic scale, emphasizing the non-exponential decay of the correlations.

Figure 3 presents the field dependence of the magnetic correlation length $l_c(H_0)$ determined from the $C(r,H_0)$ using Eq. (4). As can be seen, $l_c(H_0)$ increases from about 14 nm at the highest field of 4 T to 26 nm at the lowest field of 0.1 T. Moreover, for all fields investigated, the values of $l_c(H_0)$ remain much smaller than the average crystallite size of 60 nm of

the HPT Ni sample. This latter observation thus indicates the presence of spin-misalignment correlations on a scale smaller than the average crystallite size. From the nonlinear least squares fit of the $l_c(H_0)$ data to Eq. (5) (dashed line in Fig. 4), the following best-fit parameters are obtained: $\mathcal{L} = 11.3 \pm 0.1$ nm and $\mu_0 H^* = 71.2 \pm 3.0$ mT. We reemphasize that $\mathcal{L}$ can be regarded as an estimate of the average defect size and H^* models the influence of the magnetostatic and magnetic anisotropy field contributions to the internal magnetic field. The estimated "defect size" $\mathcal{L} \sim 11$ nm suggests that the origin of the spin misalignment observed in HPT Ni results from a high density of crystal defects on a scale smaller than the grain size, as previously suggested in HPT Fe [16]. In the remanent state, we estimate the penetration depth $\delta = l_c(H_0 = 0) - \mathcal{L}$ of the spin disorder into the ferromagnetic Ni-phase to be ~ 22 nm (Fig. 3). If the field H^* in Eq. (5) were exclusively due to an *effective* uniaxial magnetic anisotropy of strength K_u^{eff}, then $H^* = 2K_u^{\text{eff}}/(\mu_0 M_s)$ and the penetration depth $\delta = l_c(H_0 = 0) - \mathcal{L}$ would be related to the domain-wall width $\delta_w \propto \sqrt{A_{ex}/|K_u^{\text{eff}}|}$. Using $A_{ex} = 8.5$ pJ/m and assuming the (magnetocrystalline) single-crystal value of $K_u^{\text{eff}} = -5.7$ kJ/m^3 [27] (ignoring that fcc Ni has a cubic rather than an uniaxial anisotropy symmetry), we obtain $\delta_w \cong 39$ nm. On the other hand, using $A_{ex} = 8.5$ pJ/m and demanding that $\sqrt{A_{ex}/K_u^{\text{eff}}} = 22$ nm, as is experimentally found, we estimate $K_u^{\text{eff}} \cong 1.8 \times 10^4$ J/m^3. This corresponds to an increase by a factor of about 4 compared to the (magnetocrystalline) value reported in Ni single crystal. In line with the HPT process and with the finding of an increased coercivity, the above value of K_u^{eff} indicates a significant contribution to the magnetic anisotropy due to magnetoelastic effects; this hypothesis is consistent with the strain observed in the HPT sample The value of $2K_u^{\text{eff}}/M_s$ self-consistently evaluates to $\mu_0 H^* \cong 73$ mT (using $M_s = 482$ kA/m and assuming a mass density of 8.912 g/cm^3]), in agreement with the experimental result.

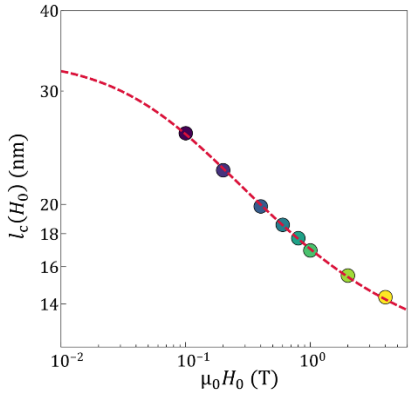

Figure 3: Field dependence of the magnetic correlation length $l_c(H_0)$, determined from the computed $C(r, H_0)$ data shown in Fig. 2 (log-log scale). Dashed line: Fit of the $l_c(H_0)$ data using Eq. (5).

4. Conclusion

We employed unpolarized magnetic SANS to investigate the influence of crystal defects on the magnetic microstructure and the macroscopic magnetic properties of nanocrystalline Ni prepared by HPT. The analysis of the field-dependent magnetic SANS data suggests the presence of strong spin misalignment on the mesoscopic length scale. In fact, the computation of the magnetic correlation function and the correlation length confirmed the presence of spin disorder on a scale smaller than the average crystallite size of 60 nm. The phenomenological model, Eq. (5), provides an excellent description of the field dependence of the spin-misalignment correlation length. We estimated the defect size to be around 11 nm and the penetration depth of the spin misalignment into the pure Ni phase in the remanent state to be around 22 nm. Under certain assumptions, the analysis of the penetration depth allows one to conclude on the magnitude of the effective magnetic anisotropy. For HPT Ni, we find an increased anisotropy (factor of 4), presumably due to magnetoelastic interactions, relative to the single-crystalline ground state. Our findings are supported by micromagnetic simulations which highlight that microstructural defects (such as pores) can induce significant nanoscale spin disorder, representing a contrast for magnetic SANS. The presented neutron-data analysis procedure is particularly useful for defect-rich materials and may pave the way to tune magnetic properties through defect engineering as proposed *e.g.* for magnetic nanostructured materials such as nanoparticles [28].

Acknowledgement

The authors acknowledge the Institut Laue-Langevin, Grenoble, France, and the Australian Nuclear Science and Technology Organization, Lucas Heights, Australia, for the provision of neutron beamtime. The authors thank Dr. Robert Cubitt for the technical support during the neutron experiments at the Institut Laue-Langevin. Andreas Michels and Evelyn Pratami Sinaga acknowledge financial support from the National Research Fund of Luxembourg (Pride MASSENA Grant No. 10935404). Yojiro Oba thanks KAKENHI (Grant No. 19K05102), the Japan Science and Technology Agency (JST) (Grant No. JPMJSK1511), and the travel expenses support of the Institute for Solid State Physics, University of Tokyo.

References

[1] A. Makino, T. Hatanai, Y. Naitoh, T. Bitoh, A. Inoue, and T. Masumoto, IEEE Trans. Magn. **33**, 3793 (1997).
[2] M. E. McHenry, M. A. Willard, and D. E. Laughlin, Prog. Mater. Sci. **44**, 291 (1999).
[3] J. Petzold, J. Magn. Magn. Mater. **242**–**245**, 84 (2002).
[4] Y. Huang and T. G. Langdon, Mater. Today **16**, 85 (2013).
[5] C. C. Koch, J. Mater. Sci. **42**, 1403 (2007).
[6] K. Edalati and Z. Horita, Mater. Sci. Eng. A **652**, 325 (2016).
[7] K. Y. Mulyukov, G. F. Korznikova, R. Z. Abdulov, and R. Z. Valiev, J. Magn. Magn. Mater. **89**, 207 (1990).
[8] K. Y. Mulyukov, S. B. Khaphizov, and R. Z. Valiev, Phys. Status Solidi **133**, 447 (1992).
[9] G. F. Korznikova, K. Y. Mulyukov, V. N. Timofeyev, and R. Z. Valiev, J. Magn. Magn. Mater. **135**, 46 (1994).
[10] G. F. Korznikova, J. Microsc. **239**, 239 (2010).
[11] C. M. Cepeda-Jiménez, J. I. Beltrán, A. Hernando, M. A. García, F. Ynduráin, A. Zhilyaev, and M. T. Pérez-Prado, Acta Mater. **123**, 206 (2017).
[12] S. Scheriau, M. Kriegisch, S. Kleber, N. Mehboob, R. Grössinger, and R. Pippan, J. Magn. Magn. Mater. **322**, 2984 (2010).
[13] Z. Horita and K. Edalati, Mater. Trans. **61**, 2241 (2020).
[14] A. Michels, J. Phys. Condens. Matter **26**, 383201 (2014).
[15] S. Mühlbauer, D. Honecker, E. A. Périgo, F. Bergner, S. Disch, A. Heinemann, S. Erokhin, D. Berkov, C. Leighton, M. R. Eskildsen, and A. Michels, Rev. Mod. Phys. **91**, 015004 (2019).
[16] Y. Oba, N. Adachi, Y. Todaka, E. P. Gilbert, and H. Mamiya, Phys. Rev. Res. **2**, 033473 (2020).
[17] D. Mettus and A. Michels, J. Appl. Crystallogr. **48**, 1437 (2015).
[18] A. Michels, Phys. Rev. B **82**, 024433 (2010).
[19] D. Honecker and A. Michels, Phys. Rev. B **87**, 224426 (2013).
[20] A. Michels, J. Weissmüller, and R. Birringer, Eur. Phys. J. B **29**, 533 (2002).
[21] J. Weissmüller, R. D. McMichael, A. Michels, and R. D. Shull, J. Res. Natl. Inst. Stand. Technol. **104**, 261 (1999).
[22] J. Weissmüller, A. Michels, J. G. Barker, A. Wiedenmann, U. Erb, and R. D. Shull, Phys. Rev. B **63**, 214414 (2001).
[23] J. P. Bick, D. Honecker, F. Döbrich, K. Suzuki, E. P. Gilbert, H. Frielinghaus, J. Kohlbrecher, J. Gavilano, E. M. Forgan, R. Schweins, P. Lindner, R. Birringer, and A. Michels, Appl. Phys. Lett. **102**, 022415 (2013).
[24] A. Michels, R. N. Viswanath, J. G. Barker, R. Birringer, and J. Weissmüller, Phys. Rev. Lett. **91**, 267204 (2003).
[25] D. Honecker, C. D. Dewhurst, K. Suzuki, S. Erokhin, and A. Michels, Phys. Rev. B **88**, 094428 (2013).
[26] G. Porod, in *Small Angle X-Ray Scatt.*, edited by O. Glatter and O. Kratky (Academic Press, London, 1985), pp. 17–51.
[27] Sōshin Chikazumi, *Physics of Magnetism* (New York, Wiley, 1964).
[28] A. Lak, S. Disch, and P. Bender, Adv. Sci. **2002682**, (2021).